Nanoscale

Accepted Manuscript

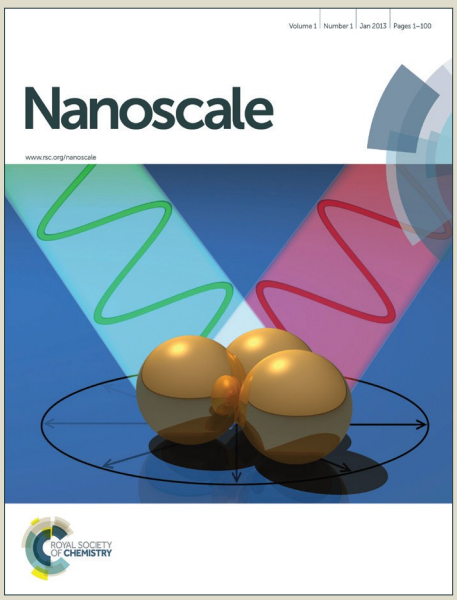

ROYAL SOCIETY OF CHEMISTRY

www.rsc.org/nanoscale

Nanoscale

Paper

Multifunctional Nitrogen-doped Graphene Nanoribbon Aerogels for Superior Lithium Storage and Cell Culture

Received 00th January 20xx,
Accepted 00th January 20xx

DOI: 10.1039/x0xx00000x

www.rsc.org/

Yang Liu,[a] Xuzhen Wang*,[a] Wubo Wan,[b] Lingli Li,[c] Yanfeng Dong,[a] Zongbin Zhao,[a] Jieshan Qiu[a]

Nitrogen-doped graphene nanoribbon aerogels (N-GNRAs) are fabricated through self-assembly of graphene oxide nanoribbons (GONRs) combined with a thermal annealing process. Amino-groups are grafted to the surface of graphene nanoribbons (GNRs) by an epoxy ring-opening reaction. High nitrogen doping level (7.6 atm% as confirmed by elemental analysis) is achieved during thermal treatment resulting from functionalization and the rich edge structures of GNRs. The three dimensional (3D) N-GNRAs feature a hierarchical porous structure. The quasi-one dimensional (1D) GNRs act as the building blocks for the construction of fishnet-like GNR sheets, which further create 3D frameworks with micrometer-scale pores. The edge effect of GNRs combined with nitrogen doping and porosity give rise to good electrical conductivity, superhydrophilic, highly compressible and low density of the GNRAs. As a result, a high capacity of 910 mAh g^{-1} is achieved at a current density of 0.5 A g^{-1} when they are tested as anode materials for lithium ion batteries. Further cell culture experiment with the GNRAs as human medulloblastoma DAOY cell scaffold demonstrates their good biocompatibility, inferring potential applications in biomedical field.

Introduction

Graphene nanoribbons (GNRs), a quasi-one dimensional (1D) form of graphene, have attracted extensive attentions due to their special structures and excellent physicochemical properties. Like the single wall carbon nanotubes, GNRs would be metallic if they have zigzag edges, while armchair edges give rise to either semiconducting or metallic transport.[1,2] But unlike the seamless structure of carbon nanotubes (CNTs), the surface of GNRs is opened graphitic plane with enormous reactive edges which could enhance the adsorption and electrocatalysis of certain molecules.[3] For example, both computation modeling and experiments have proved that the adsorption of lithium ions could be enhanced due to the edge effect of GNRs.[4,5] And the electronic and chemical properties of GNRs could be further modified through nitrogen doping.[6] Up to now, many methods have been developed to synthesize GNRs or nitrogen doped GNRs (N-GNRs). Longitudinal cutting of CNTs is believed to be the most promising way to produce GNRs on large scale.[1] The wet chemical method using H_2SO_4 and $KMnO_4$ as oxidizing agent to break the C-C bonds of tube walls has been developed by Kosynkin et al.[7] Graphene oxide nanoribbons (GONRs) with large amount of oxygen containing functional groups (i.e. epoxy, carbonyl, and carboxyl groups) were produced during the strong oxidation process. This chemical method was also used to unzip nitrogen doped CNTs but the nitrogen content sharply reduced as the doped sites were more vulnerable to oxidant.[8]

Assembling of carbon nanomaterials like CNTs or graphene into macroscopic structures is thought to be a critical procedure to realize their practical applications. The fabrication of GNRs into fiber (1D),[9] yarn (1D) and sheet (two dimensional, 2D)[10] have been realized. And approaches such as unzipping of CNT sponge,[11] hydrothermal mediated assembly of GONRs[12-14] have also been developed to construct three dimensional (3D) graphene nanoribbon aerogel (GNRA) or nitrogen-doped graphene nanoribbon aerogel (N-GNRA). However, more efficient ways for the preparation of N-doping GNRA with high nitrogen content and novel properties at mild condition are still strongly desirable.

In addition to rational design and synthesis of carbon materials with certain structures, it is also very important to realize their proper applications. Due to the high electrical conductivity, large surface area and nanostructures, CNTs and graphene have been investigated as anode materials for lithium ion batteries (LIBs),[15] and their lithium storage abilities can be further improved through nitrogen doping due to the improvement of reactivity and electrical conductivity of carbon materials.[16-18] However, there are few investigations about lithium storage ability test of GNRs or N-GNRs. Furthermore, there has been a tremendous interest in applying the carbon materials for potential biological applications owing to their inherent biocompatibility.[19] And in the field of tissue engineering, the 3D carbon materials with strong mechanical properties and porous structures make them promising candidates to be used as cell culture scaffold.[20] Nevertheless, many CNT foams or graphene

[a] Carbon Research Laboratory, Liaoning Key Lab for Energy Materials and Chemical Engineering & School of Chemistry, State Key Lab of Fine Chemicals, Faculty of Chemical, Environmental and Biological Science and Technology, Dalian University of Technology, Dalian, 116024, China. E-mail:xzwang@dlut.edu.cn
[b] College of Biological and Environmental Engineering, Zhejiang University of Technology, Hangzhou, Zhejiang 310032, China.
[c] School of Optometry & Ophthalmology, Wenzhou Medical University, Wenzhou 325000, P. R China
†Electronic supplementary information (ESI) available.
SeeDOI: 10.1039/x0xx00000x

aerogels exhibit hydrophobic property which makes the infiltration of cell culture fluid difficult.[21,22] So it is necessary to synthesize 3D carbon aerogels with hydrophilic surface to realize their biological applications.

As mentioned above, GONRs are the oxidized form of GNRs that possess abundant oxygen containing functional groups on their edge and plane which make them suitable precursor to construct macro structures like graphene oxide.[23] Herein, functionalization with ethylenediamine (EDA) combined with thermal annealing was designed to build N-GNRAs with novel hierarchical structure. Benefitted from the edge effect, hierarchical porous nanostructures, high N doping content and superhydrophilic surface property, they exhibit excellent performance both in the storage of lithium ions and human cell culture.

Experimental

Synthesis of CNTs

CNTs were synthesized through a pump injection chemical vapor deposition process with ferrocene as catalyst precursor and toluene as carbon source. Briefly, a solution of ferrocene dissolved in toluene (5wt%) was prepared then inhaled into a syringe driven by a pump. The solution was injected into a quartz tube which was placed into tubular furnace at a fixed feeding rate (0.15 mL min^{-1}). The ferrocene and toluene evaporated at the entrance of tubular furnace and was carried to the high temperature region by the mixture of hydrogen and argon (H_2 100 sccm, Ar 400 sccm). The whole reaction lasted for 1 h at temperature of 800 ^{o}C then cooled down naturally to room temperature (RT) at the protection of argon. The CNTs were collected at the inner walls of quartz tube then purified by nitric acid solution (8 mol L^{-1}) at 80 ^{o}C for 4h.

Unzipping process of CNTs

The obtained purified CNTs were unzipped with H_2SO_4 and $KMnO_4$ as oxidants as previously reported.[7] In brief, CNTs (1.0 g) were added into concentrated H_2SO_4 (130 mL) and sonicated for 0.5 h to evenly distribute them. The formed mixture was stirred for 1h at RT with a mechanical agitator. Subsequently, $KMnO_4$ (5.0 g) was slowly added and the reaction lasted for 1 h at RT. Finally, the solution was kept at 70 ^{o}C for 2 h. After the reaction, the obtained brown solution was slowly poured into ice water (500 mL) containing H_2O_2 (10 mL, 30 wt%). The GONRs was centrifuged and washed with deionized water for five times and re-dispersed in water to form a homogeneous dispersion.

Preparation of N-GNRA

EDA (20μl) was added into GONRs dispersion (4 mg mL^{-1}, 5 mL) and sonicated for 1 min to uniformly mix with each other. Soon afterwards, the mixture was sealed in a glass vial and heated for 6 h at 95 ^{o}C to form GNR hydrogel. After freeze-drying, GNRA functionalized with amino-groups was obtained. After the high temperature annealing treatment at 800 ^{o}C for 1h with Ar as protective gas, the final N-GNRA was produced.

Characterization

The morphology of products was characterized by scanning electron microscopy (SEM, JMS-6360 LV), field-emission scanning electron microscopy (FESEM, QUANTA 450, 20KV) Atomic Force Microscope (AFM, Dimension Icon) and transmission electron microscopy (TEM, JEM-2000EX). The crystalline phases of the products were examined using Rigaku D/MAX-2400 diffractometer (XRD) equipped with a rotating anode and a CuKα radiation source (λ=0.15418 nm). Elemental analysis (Vario EL III) was used to determine the elemental composition of the samples. Fourier transform infrared spectroscopy (FTIR, EQUINOX55) was used to analyze the attached functional groups. X-ray photoelectron spectroscopy (XPS) analysis was performed using a Thermo ESCALAB 250 spectrometer employing an Al-Kα X-ray source. Raman spectroscope (JYLabRam HR800, excited by 633 nm laser) was used to analyse the defects on the carbon materials. The specific surface area and pore size distribution were examined by nitrogen adsorption/desorption (Micromeritics ASAP2020 instrument). Thermal stability of the samples was assessed by thermal gravimetric analysis (TGA, TA-Q50). The contact angle was measured on an OCA20 machine (Data-Physics, Germany).

Electrochemical measurements

At first, slurry was prepared by mixing 70wt% active electrode material (N-GNRA), 20wt% acetylene black, 10wt% polyvinylidene fluoride (PVDF) binder. Then a working electrode was fabricated by slurry casting on a Cu foil. The electrodes were dried under vacuum at 120 ^{o}C overnight. Coin type cells were assembled in a glove box under argon atmosphere (water and oxygen concentration less than 0.1 ppm). It consisted of a prepared electrode, polypropylene separator, and lithium foil as the counter electrode. The electrolyte used in this experiment was 1 M $LiPF_6$ salt dissolved in ethylene carbonate (EC), diethyl carbonate (DEC) in a 1:1 volume ratio. The galvanostatic charge/discharge tests were carried out on a Land CT2001A battery test system between 0.01–3.0 V using 2016 coin-type cells. The cyclic voltammograms (CV) and electrochemical impendence spectra (EIS) were conducted using a multichannel electrochemical workstation (VMP-300).

Cell culture

N-GNRA was cut into discs with diameter of 10 mm and thickness of 2 mm. Then samples were sterilized by being exposed in UV light for 1 h, immersed into 75% ethanol overnight, followed by washing with phosphate buffer solution (PBS) for 3 times and soaked in culture media overnight. The samples were seeded with 2×104 human medulloblastoma DAOY cells per well, and cultured in Dulbecco's Modified Eagle Medium (Gibco, Life Technologies, USA), supplemented with 10% Fetal Bovine Serum (Gibco, Life Technologies, USA), 1% Penicillin-Streptomycin (Gibco, Life Technologies, USA) at 37 ^{o}C in 5% CO_2. After 24 h and 72 h, the cells were stained with Calcein AM, which is cleaved to yield a green fluorescent

product by metabolically active cells and red fluorescent product by dead cells, respectively. Calcein AM (green for live cells) and ethidium homodimer-1 (red for dead cells) were added to PBS at a concentration of 0.5 and 2 μl mL^{-1}. The samples were then placed into the incubator for 30 min. Images were obtained using a Nikon Eclipse Ti microscope and analyzed by Image J software.

Results and discussion

Preparation of nitrogen doped graphene nanoribbon aerogel (N-GNRA)

The overall synthetic procedure of N-GNRA is shown in Fig. 1, which mainly involves three steps. Firstly, the as-prepared CNTs were unzipped into GONRs through a longitudinal cutting and oxidation process by H_2SO_4/$KMnO_4$. Secondly, EDA was introduced to functionalize GONRs via epoxy ring-opening reaction and simultaneously induce the self-assembly of GONRs. Finally, high temperature annealing process was taken to eliminate the residual oxygen-containing groups and decompose the nitrogen-containing functional groups for the formation of N-GNRA.

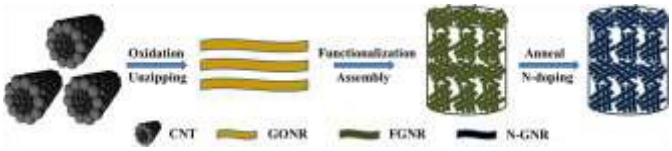

Fig. 1 Schematic illustration for the construction of 3D N-GNRA.

The detailed self-assembly process and morphology transformation from GONRs to N-GNRA are shown in Fig. S1-3 and Fig. 2. As shown in Fig. S1 and Fig. 2b,c, CNTs with the average diameter of 43 nm and length of ~200 μm were prepared with chemical vapor deposition method. Then they were fully unzipped to produce GONRs with high aspect ratio and good dispersibility in water (Fig. 2d and Fig. S2a-c). The average thickness of GONRs is 18.5 nm (Fig. S2d-g). EDA was introduced to functionalize the GONRs and initiated their cross-linking. The brown GONR dispersion turned black and then became sticky gradually. Finally it was transformed into hydrogel after heating for 6 h at 95 ^{o}C (Fig. S3). The critical concentration to form monolithic structure was found to be about 4 mg mL^{-1} (Fig. S4). The as-prepared GNR hydrogel was freeze dried to form functionalized GNR aerogel (FGNRA).

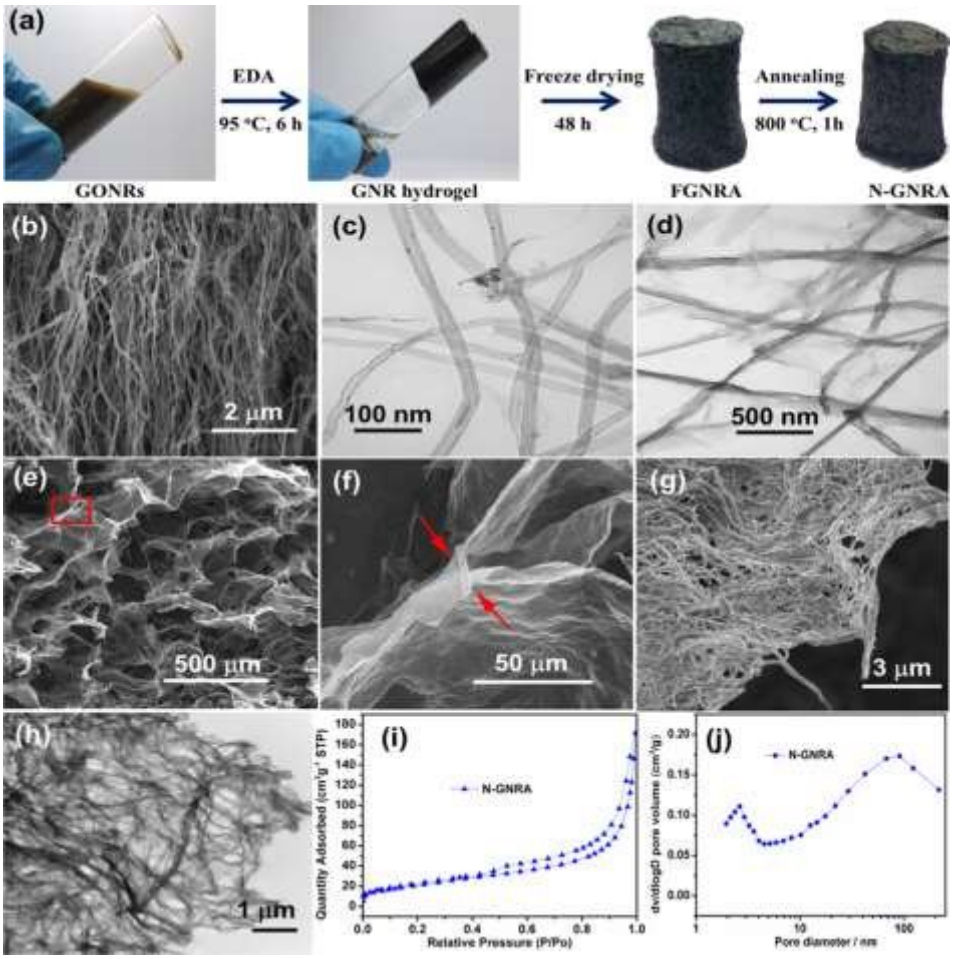

Fig. 2 a) Digital photographs of the transformation of GONRs to N-GNRA. b) SEM image and c) TEM image of pristine CNTs. d) TEM image of GONRs. e) SEM image of N-GNRA. f) enlarged image of e). g) SEM image and h) TEM image of N-GNRA. i) Nitrogen adsorption and desorption isotherm of N-GNRA. j) Pore-size distribution of N-GNRA.

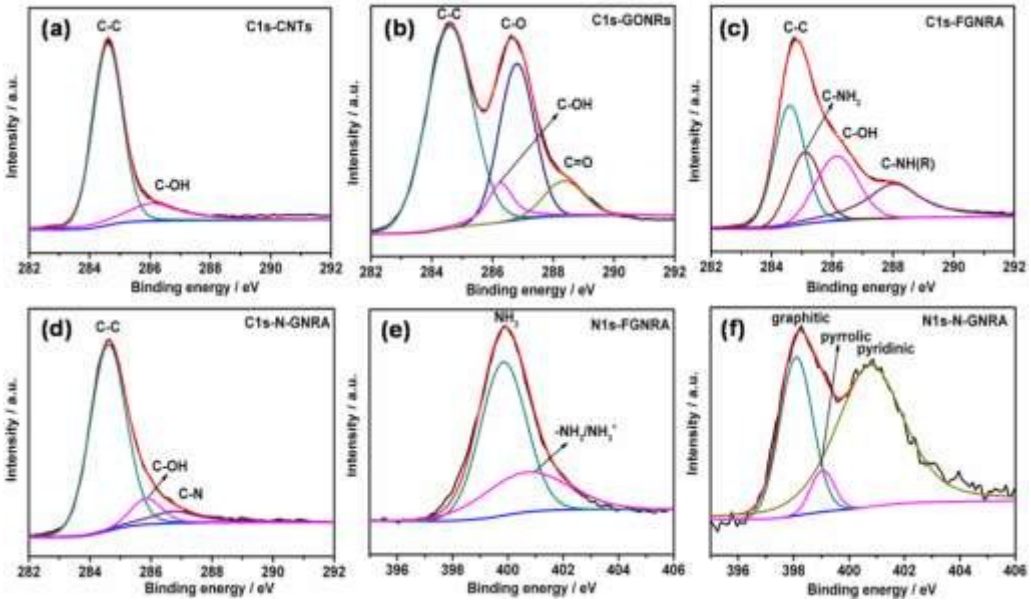

Fig. 3 XPS of C1s spectra of a) pristine CNTs; b) GONRs; c) FGNRA and d) N-GNRA. e, f) N1s spectra of e) FGNRA and f) N-GNRA.

Then final N-GNRA was obtained after a thermal annealing process at 800 °C.

The resultant aerogels have a black and foam-like appearance. Different from the jumbled stack of GNRs in GNRA synthesized by other methods,[11-14] our 3D N-GNRA is constructed by large amount of interconnected 2D sheet-like structures with pores ranging from tens to hundreds of micrometer as shown by SEM images (Fig. 2e). The magnified image (Fig. 2f) of the selected area displays two different sheets that are closely connected together with long boundaries up to tens of micrometers (the point of junction is marked by red arrows). SEM (Fig. 2g and Fig. S2h) and TEM (Fig. 2h and Fig. S2j) images are used to exhibit their nanostructures. Fig. 2g,h and Fig. S2e,f show that these sheets are consisted of flat GNRs with average diameter of 121 nm which is about three times the diameter of CNTs. The formation of 2D GNR sheets could be ascribed to the growth of ice crystals. During the freezing, GNRs are located in a confined space between the adjacent of ice crystals then macroporous monolith structures composed of thin GNR sheets are formed after lyophilization.[24,25] SEM (Fig. 2g) and TEM images (Fig. 2h) also feature nanoscale pores distributed on the 2D GNR sheets. Nitrogen adsorption and desorption show a typical Type Ⅱ isotherm with an adsorption hysteresis loop (Fig. 2i), indicating mesopores and macropores in the aerogels. Due to the exposure of inner space and pores, the BET surface area of GNRA (78.9 m^2 g^{-1}) is higher than that of the pristine CNTs (49.6 m^2 g^{-1}, Fig. S1e). No doubt, activation can further increase the specific surface area of N-GNRA[26]. The pore size distribution is calculated by the BJH method (Fig. 2j), which exhibits two concentrated peaks that locate at the pore diameter of 2.6 and 90 nm respectively. The mesopores produced during the freeze drying process have also been observed in graphene aerogels.[27] And the second peak located at macroporous region is formed by the weave of GNRs, which is in accordance with the SEM and TEM observation.

A series of characterizations including X-ray diffraction (XRD, Fig. S5), X-ray photoelectron spectra (XPS, Fig. 3), elemental analysis (Fig. S6) and Fourier transform infrared spectroscopy (FTIR, Fig. S7) have been conducted in order to understand the compositions and structures of N-GNRA. As shown in Fig. S5, the pristine CNTs show a typical graphite (002) peak at $2\theta = 25.9^{o}$, which means the *d* spacing of CNTs is 3.4 Å, similar to that of graphite. However, the peak shifts to $2\theta = 8.5^{o}$ after the oxidation process, corresponding to the increase of the interlayer space to 10.4 Å, indicating the successful exfoliation of the CNTs. While there are no obvious diffraction peaks in the XRD patterns of FGNRA, indicating the reduction of GONRs and the separation of GNR layers. Similarly, there is no significant peak in the XRD profiles of N-GNRA.

XPS was used to identify the functional groups and nitrogen content of the products (Fig. 3). There are C-C (284.6 eV) and weak C-OH (286.1 eV) peaks in the pristine CNTs, which could be ascribed to the sp^2-hybridized carbon and chemically adsorbed water.[28] After the oxidation process, C-O (epoxy or alkoxy), C=O (carbonyl or carboxyl) groups appear, which locate at 286.8 eV and 288.4 eV respectively in the C1s spectra of GONRs.[7,29] And the low C/O ratio of 2.4 (Fig. S6b, c) suggests there are large amount of oxygen functional groups in the GONRs which bring about them well dispersed in water. C1s and N1s spectra of FGNRA show that C-O and C=O groups disappear while C-NH_2 (285.1 eV), C-NH(R) (288.0 eV) groups arise after the functionlization/assembly procedure.[30,31] This can be attributed to the functionalization from EDA, which can partially reduce GONRs and introduce amine groups into the samples through a nucleophilic ring-opening reaction of epoxy groups on the planes of GONRs.[30,32] The functional groups are subsequently removed through annealing treatment as shown

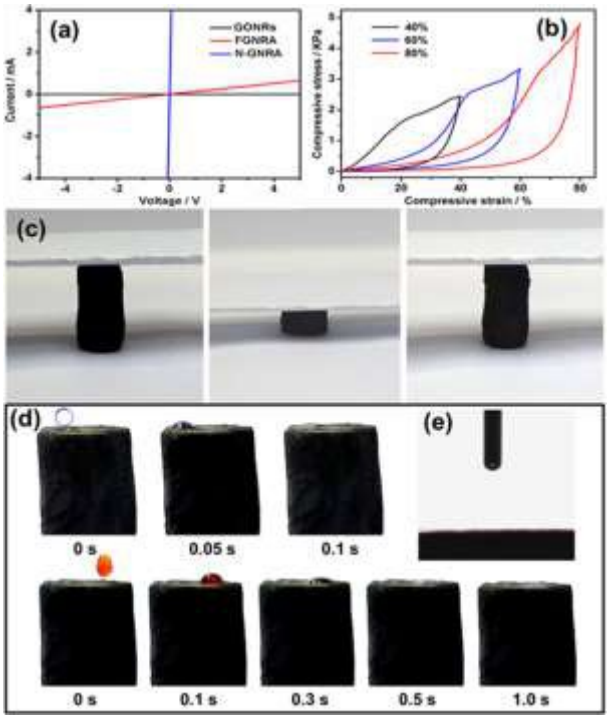

Fig. 4 a) Room temperature I-V curves of GONRs, FGNRA and N-GNRA. b) The stress-strain curves of N-GNRA at different maximum strain of 40%, 60%, 80%. c) Digital images show the compressibility of N-GNRA. d) Digital images reveals the superhydrophilicity and superoleophilicity of N-GNRA (the transparent droplet marked by a circle is DI water add on the left side of aerogel. While the red one is vegetable oil labeled with Sudan Ⅲ drip into the right side). e) N-GNRA shows superhydrophilicity with a water contact angle of nearly 0°.

in Fig. 3d. As a result, the nitrogen in the amine groups could be integrated Into GNRs to give rise to nitrogen doped GNRs, i.e. N-GNRs.

The N1s spectra of N-GNRA demonstrate three types of nitrogen namely graphitic (398.1 eV), pyrrolic (399.0 eV) and pyridinic (400.8 eV) nitrogen.[16-18,33] The N/C ratio is 7.6 atm% (average value based on three different samples) provided by elemental analysis (Fig. S6a,c), indicating successfully doping of N into the carbon framework of GNRs with a high content. The nitrogen element evenly disperses in the GNR sheets, which is confirmed by the elemental mapping (Fig. S7). The transformation of functional groups during thermal annealing has also been analyzed by FTIR and the results are shown in Fig. S8, which are consistent with XPS. The efficient nitrogen doping process can be ascribed to the formation of C-N bonds during the ring-opening reaction which is favorable for N doping.[34] Moreover, the abundant edges in GNRs are conducive to high N doping level since the edge carbon atoms are more easily substituted with N atoms.[6,35]

Thermal stability and structure changes of all samples were further investigated by thermal gravimetric analysis (TGA, Fig. S9a), differential thermal analysis (DTA, Fig. S9b) and Raman spectra (Fig. S9c). The weight percent loss of N-GNRA is 6 wt%, much less than the 40 wt% of FGNRA or 56 wt% of GONRs as the temperature reaches 400 °C. This result further confirms that most of functional groups have been detached from GNRs after thermal treatment. Raman spectra are used to identify the structural differences between samples. The D and G band locates around 1328 and 1590, respectively (Fig. S9c). The I_D/I_G ratio of CNTs is 0.65 and increases to 1.27 after the longitudinal unzipping process resulting from the increasing of defects. While the I_D/I_G ratio of FGNRA slightly rises to 1.38 owing to the increase number of small domains of aromaticity.[7,29] And more defects are introduced into the structures during the nitrogen doping process as the N-GNRA has the highest I_D/I_G ratio of 1.49.

The physicochemical properties of N-GNRA

The density of typical as-prepared aerogel is 6.7 mg cm^{-3} within the scope of ultralight material (10 mg cm^{-3}).[36] And its density can be easily tuned by adding different amount of EDA without changing the concentration of GONRs' dispersion (Fig. S10). The GONRs is electrically insulated due to the existence of abundant oxygen functional groups (Fig. 4a). After functionalization with EDA, the FGNRA shows increased conductivity of 2.1×10^{-4} S cm^{-1}, resulting from the partial reduction and restoration of sp^2 in the carbon substrate. However, the electrical conductivity of N-GNRA increases to 1.4×10^{-1} S cm^{-1} which is three orders of magnitudes of FGNRA (2.1×10^{-4} S cm^{-1}) and superior to many graphene aerogels or hydrogels reported previously.[23,30] The high electrical conductivity can be ascribed to the net structures of aerogel which are favorable for electron transport. In addition to good electrical conductivity, N-GNRA also behaves elastically under compression. The stress-strain curve in Fig. 4b shows that the N-GNRA can recover to the origin shape at large compressive strain of $\varepsilon = 80$ %, which is also shown in the digital images (Fig. 4c). However, the compressibility of FGNRA is poor due to the hydrogen bonding formed within the large amount of functional groups during compression (Fig. S11).

Moreover, the wettability of N-GNRA is tested with deionized water and vegetable oil droplet. Interestingly, it is found that the aerogel exhibits both superhydrophilic and superoleophilic surface property as shown in Fig. 4d,e. The superoleophilic carbon materials have been used to absorb oil, such as CNT sponge or graphene aerogel.[21,22] However, the superhydrophilicity of carbon materials have not been well investigated. As reported by Jiang's group, the bottom of the lotus leaf and the surface of TiO_2 mesh exhibit superhydrophilicity due to the existing of micro/nano hybrid rough structures which are favorable for water storage.[37,38] So we believe that the hierarchical porous structure of N-GNRA with a micro and nano-scale 3D capillary effect plays a crucial role in the fast spreading of water droplet. According to the previous researches, materials with superhydrophilic surface always have selectively absorbing ability to capture cancer cells or used as substrate for cell culture which show good prospect in the biological and medical fields.[19,20,39,40]

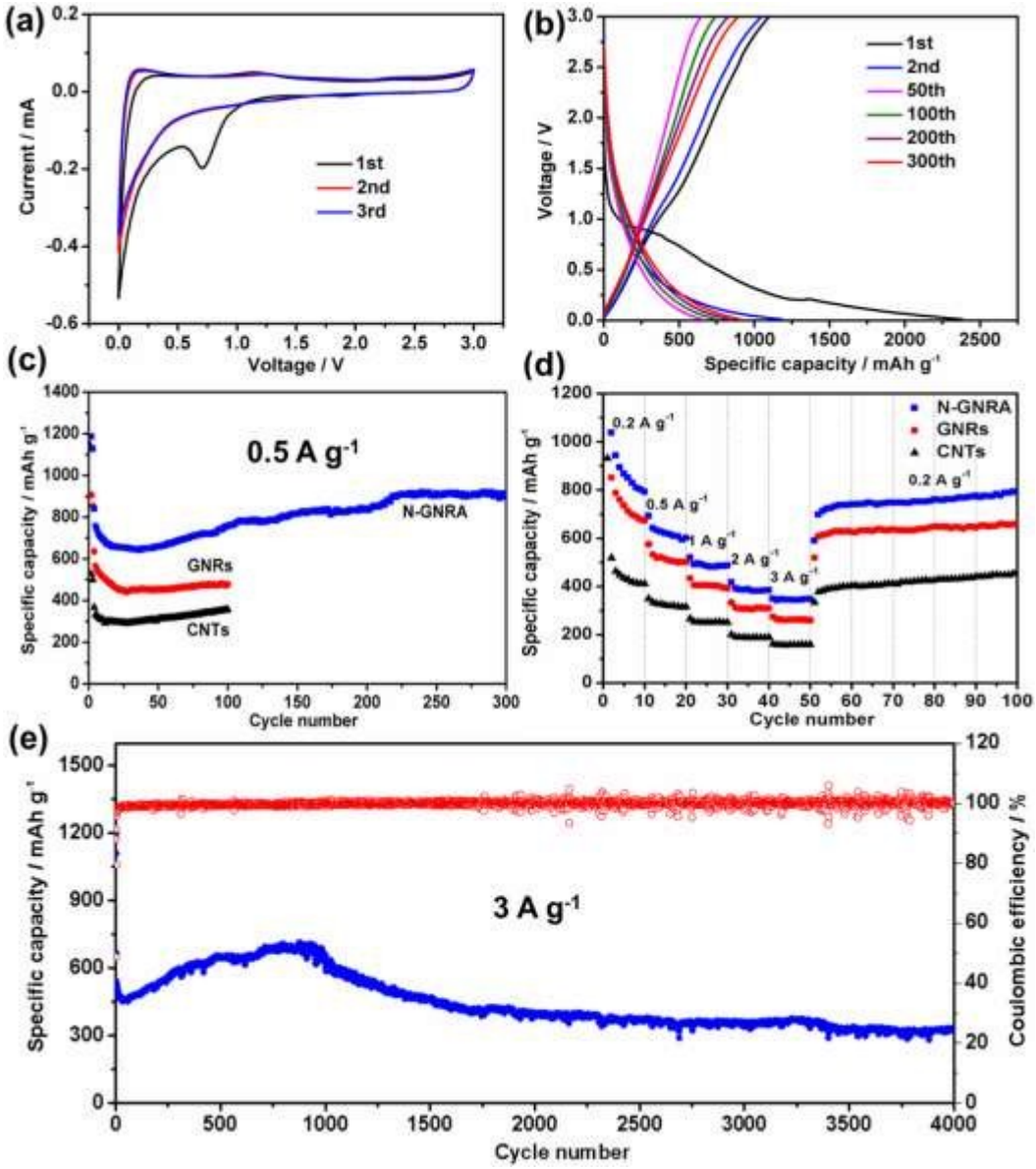

Fig. 5 a) Cyclic voltammograms (CVs) of N-GNRA, obtained at a scan rate of 0.1 mV s^{-1} between 0.01 and 3.0 V. b) Charge and discharge voltage profiles of N-GNRA. c) Comparative cycling performance of N-GNRA, GNRs and CNTs, tested at a current density of 0.1 A g^{-1} for the first three cycles then 0.5 A g^{-1} for the following cycles. d) Rate capability of N-GNRA, GNRs and CNTs tested at various current densities ranging from 0.2 A g^{-1} to 3 A g^{-1}. e) Cycling performance of N-GNRA tested at a current density of 3 A g^{-1} (the first three cycles were also tested at a current density of 0.1 A g^{-1}).

Electrochemical performance of N-GNRA anode

Based on its edge effect, porous structure, nitrogen doping and good electrical conductivity properties, the N-GNRA was used as anode materials for LIBs. Fig. 5a is cyclic voltammograms (CVs) of N-GNRA electrode between 0.01-3.0 V at a scan rate of 0.1 mV s^{-1}. There is a strong peak located between 0.5-1.0 V at the discharge brand of first cycle while disappears in the following cycles. This peak is usually attributed to the formation of solid electrolyte interphase (SEI) film induced by the occurrence of side reaction on the electrode surface or interface.[16-18,41] The discharge capacity of N-GNRA is as high as 2383 mAh g^{-1} and the reversible capacity is 1098 mAh g^{-1} for the initial cycle at current density of 0.1 A g^{-1} shown in Fig. 5b. The irreversible capacity loss can be ascribed to the inevitable formation of SEI film and electrolyte decomposition.[16-18,41] From the fourth cycle the test current density increases to 0.5 A g^{-1}, but the discharge capacity still keeps over 640 mAh g^{-1} and gradually rises to 910 mAh g^{-1} within 300 cycles (Fig. 5c).

Nitrogen doping is thought to be the main reason that induces the rising of capacity as observed in nitrogen doped CNTs and graphene.[18,42,43] In detail, nitrogen doping generates defects and vacancies on the graphene sheets through which

lithium ion could spread into the inner layers.[42] Moreover, the amount of defects and vacancies would increase during the charge and discharge process and provide more lithium storage sites.[43] The capacity of N-GNRA is higher than that of the nitrogen doped or undoped CNTs, graphene, GNRs and even higher than some metal oxide/carbon composites previously reported.[5,32,44-46] Control experiments further demonstrate the superior performance of N-GNRA for lithium storage. Various samples including GNRs (obtained by thermal treatment of GONRs without the EDA mediated assembly process), pristine CNTs and nitrogen doped graphene aerogel (N-GA, prepared by the EDA mediated assembly process and the morphology was shown in Fig. S12) were also tested as anode materials for LIBs. Discharge capacity of 476 mAh g^{-1} is retained for GNRs, much higher than that (356 mAh g^{-1}) of CNTs (Fig. 5c). This can be ascribed to the edge effect of GNRs which could enhance lithium storage, as the binding energy of Li ions on nanoribbons is comparable or even superior to those of graphene and other carbon materials confirmed by theoretical computation and experiment.[4,5] In addition, the exposure of inner tube cavities also provide more surface for lithium storage. However, the capacity of GNRs is much lower than the capacity (756 mAh g^{-1}) of N-GNRA after 100 cycles. It mainly results from the effect of nitrogen doping because Li ions are more favorable binding with nitrogen doped sites, which lead to improved lithium storage ability.[16,42] The capacity rising is also observed at the cycling performance of N-GA as the discharge capacity increase to 713 mAh g^{-1} from 528 mAh g^{-1} after 300 cycles (Fig. S13a). Compared with N-GA, the capacity of N-GNRA is relatively higher, which further confirms the edge effect of ribbon structures. It is also found the specific capacity of CNTs increased with cycles. This can be mainly ascribed to their gradual structure changes during the repeated Li^+ insertion/desertion process and has been explained by Wei et al.[47]

In addition to the capacity, superior rate capability is another important factor for high performance LIBs. The rate performance of N-GNRA is shown in Fig. 5d. Discharge capacity of 340-800 mAh g^{-1} can be retained when test at different current densities range from 0.2-3.0 A g^{-1}. After cycling at 3.0 A g^{-1}, the capacity restores to over 700 mAh g^{-1} and keeps rising from then on. Obviously, the N-GNRA shows superior rate capability to GNRs (260-670 mAh g^{-1}), CNTs (150-410 mAh g^{-1}) and N-GA (230-630 mAh g^{-1}, Fig. S13b) tested at the same current densities. In addition, long cycling performance at high current density of 3 A g^{-1} is evaluated for N-GNRA (Fig. 5e). The capacity keeps rising before 1000 cycles and reaches a maximum of 680 mAh g^{-1}. Finally, a discharge capacity of 326 mAh g^{-1} is still obtained after 4000 cycles which is comparable to the theoretical capacity (372 mAh g^{-1}) of graphite. The excellent rate and stable cycling performance benefit from the following three factors. Firstly, the connected GNR network with high electrochemical conductivity is favorable for fast electron transfer. Secondly, hierarchical porous structures supply facile transport channels for electrolyte and the diffusion of Li^+ ions.[48-50] Finally, nitrogen doping in GNRs can enhance their electrochemical reactivity and electronic conductivity (confirmed by EIS spectra as shown in Fig. S14) which contribute to their improvement of rate capability and cycling stability.[15-17]

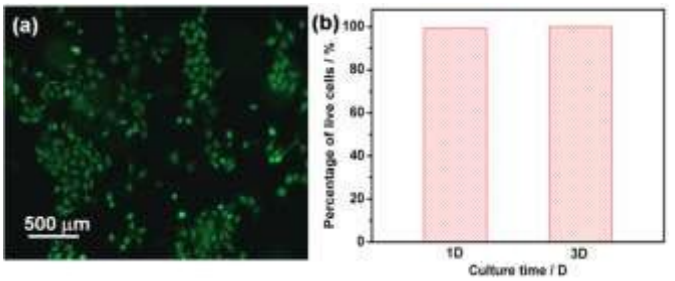

Fig. 6 a) Fluorescence micrographs of human medulloblastoma DAOY cells attached on the N-GNRA after culturing for 3 days. b) The percentage of live cells after culturing for 1 day and 3 days.

N-GNRA used as scaffold for cell culture

The superhydrophilicity and 3D self-supporting structure of N-GNRA make it potential material applied in the biomedical field. The human medulloblastoma DAOY cells were cultured on the surface of N-GNRA to take the initial cytotoxicity assay. Within 24 h, most of DAOY cells were found to attach to the N-GNRA scaffold (Fig. S15). After 3 days, DAOY cells proliferated and migrated along the skeleton of GNR sheets, and grew in a 3D fashion (Fig. 6a). Moreover, the presence of unfocused cells suggests that the DAOY cells have migrated into the N-GNRA porous structure.[51] The cell viability reached over 99% after 24 and 72 h, (Fig. 6b), showing non-cytotoxicity of N-GNRA scaffold. Thus, N-GNRA provides a good scaffold for the adhesion and proliferation of human medulloblastoma DAOY cells, suggesting potential in biomedical applications.

Conclusions

In summary, 3D N-GNRA with hierarchical porous structures was successfully constructed with GNRs as building blocks through an EDA mediated self-assembly process. The N-GNRA exhibits excellent lithium storage ability, high discharge capacity of 910 mAh g^{-1} was obtained at a current density of 0.5 A g^{-1} and discharge capacity of 326 mAh g^{-1} could still be retained after 4000 cycles at high current density of 3.0 A g^{-1}. A variety of characteristics including high electrical conductivity, nitrogen doping and porous structures, especially unique edge effect made N-GNRA a suitable anode material for high performance LIBs. Moreover, due to the superhydrophilic surface property and 3D porous structures, the N-GNRA acts as a good scaffold to culture human medulloblastoma DAOY cells. The cells migrated along the skeleton of GNR sheets and grew in a 3D fashion in the substrate. The percentage of live cells could reach over 99% after 3 days, indicating good biocompatibility and potential application in biomedical field. And we believe that the N-GNRA can also be used in fuel cells, supercapacitor and shock absorption due to its excellent electrochemical and mechanical properties.

Acknowledgements

The authors acknowledge financial supports from the National Natural Science Foundation of China (Grant No.51072028, No.21176043).

Notes and references

1 M. Terrones, *ACS Nano*, 2010, **4**, 7.
2 M. Terrones, A. R. Botello-Méndez, J. Campos-Delgado, F. López-Urías, Y. I. Vega-Cantú, F. J. Rodríguez-Macías, A. L. Elías, E. Muñoz-Sandoval, A. G. Cano-Márquez, J. C. Charlier, *Nano Today*, 2010, **5**, 351.
3 X. Jia, J. Campos-Delgado, M. Terrones, V. Meunier, M. S. Dresselhaus, *Nanoscale*, 2011, **3**, 86.
4 C. Uthaisar, V. Barone, J. E. Peralta, *J. Appl. Phys.*, 2009, **106**, 113715.
5 T. Bhardwaj, A. Antic, B. Pavan, V. Barone, B. D. Fahlman,*J. Am. Chem. Soc.*, 2010, **132**, 12556.
6 Y. Li, Z. Zhou, P. Shen, Z. Chen, *ACS Nano*, 2009, **3**, 1952.
7 D. V. Kosynkin, A. L. Higginbotham, A. Sinitskii, J. R. Lomeda, A. Dimiev, B. K. Price, J. M. Tour, *Nature*, 2009, **458**, 872.
8 R. Cruz-Silva, A. Morelos-Gomez, S. Vega-Diaz, F. Tristan-Lopez, A. L. Elias, N. Perea-Lopez, H. Muramatsu, T. Hayashi, K. Fujisawa, Y. A. Kim, *ACS Nano*, 2013, **7**, 2192.
9 C. Xiang, N. Behabtu, Y. Liu, H. G. Chae, C. C. Young, B. Genorio, D. E. Tsentalovich, C. Zhang, D. V. Kosynkin, J. R. Lomeda, *ACS Nano*, 2013, **7**, 1628.
10 J. Carretero-Gonzalez, E. Castillo-Martinez, M. Dias-Lima, M. Acik, D. M. Rogers, J. Sovich, C. S. Haines, X. Lepro, M. Kozlov, A. Zhakidov, Y. Chabal, R. H. Baughman, *Adv. Mater.*, 2012, **24**, 5695.
11 Q. Peng, Y. Li, X. He, X. Gui, Y. Shang, C. Wang, W. Zhao, S. Du, E. Shi, P. Li, D. Wu, A. Cao, *Adv. Mater.*, 2014, **26**, 3241.
12 L. Chen, R. Du, J. Zhu, Y. Mao, C. Xue, N. Zhang, Y. Hou, J. Zhang, T. Yi, *Small*, 2015, **11**, 1423.
13 Y. Gong, H. Fei, X. Zou, W. Zhou, S. Yang, G. Ye, Z. Liu, Z. Peng, J. Lou, R. Vajtai, B. I. Yakobson, J. M. Tour, P. M. Ajayan, *Chem. Mater.*, 2015, **27**, 1181.
14 L. Chen, C. Xu, R. Du, Y. Mao, C. Xue, L. Chen, L. Qu, J. Zhang, T. Yi, *J. Mater. Chem. A,* 2015, **3**, 5617.
15 N. A. Kaskhedikar, J. Maier, *Adv. Mater.*, 2009, **21**, 2664.
16 Z. S. Wu, W. Ren, L. Xu, F. Li, H. M. Cheng, *ACS Nano*, 2011, **5**, 5463.
17 F. Zheng, Y. Yang, Q. Chen, *Nat. Commun.*, 2014, **5**, 5261.
18 J. Hou, C. Cao, F. Idrees, X. Ma, *ACS Nano*, 2015, **9**, 2556.
19 H. Chen, M. B. Müller, K. J. Gilmore, G. G. Wallace, D. Li, *Adv. Mater.*, 2008, **20**, 3557.
20 N. Li, Q. Zhang, S. Gao, Q. Song, R. Huang, L. Wang, L. Liu, J. Dai, M. Tang, G. Cheng, *Sci Rep.*, 2013, **3**, 1604.
21 X. Gui, J. Wei, K. Wang, A. Cao, H. Zhu, Y. Jia, Q. Shu, D. Wu, *Adv. Mater.*, 2010, **22**, 617.
22 H. Sun, Z. Xu, C. Gao, *Adv. Mater.*, 2013, **25**, 2554.
23 Y. Xu, K. Sheng, C. Li, G. Shi, *ACS Nano*, 2010, **4**, 4324.
24 J. Zou, J. Liu, A. S. Karakoti, A. Kumar, D. Joung, Q. Li, S. I. Khondaker, S. Seal, L. Zhai, *ACS Nano*, 2010, **4**, 7293.
25 L. Qiu, J. Z. Liu, S. L. Chang, Y. Wu, D. Li, *Nat. Commun.*, 2012, **3**, 1241.
26 Z. Juanjuan, L. Ruiyi, L. Zaijun, L. Junkang, G. Zhiguo, W. Guangli, *Nanoscale*, 2014, **6**, 5458.
27 X. Zhang, Z. Sui, B. Xu, S. Yue, Y. Luo, W. Zhan, B. Liu, *J. Mater. Chem.*, 2011, **21**, 6494.
28 V. Datsyuk, M. Kalyva, K. Papagelis, J. Parthenios, D. Tasis, A. Siokou, I. Kallitsis, C. Galiotis, *Carbon*, 2008, **46**, 833.
29 A. L. Higginbotham, D. V. Kosynkin, A. Sinitskii, Z. Sun, J. M. Tour, *ACS Nano*, 2010, **4**, 2059.
30 H. Hu, Z. Zhao, W. Wan, Y. Gogotsi, J. Qiu, *Adv. Mater.*, 2013, **25**, 2219.
31 C. Zhang, R. Hao, H. Liao, Y. Hou, *Nano Energy,* 2013,**2**, 88.
32 J. Che, L. Shen, Y. Xiao, *J. Mater. Chem.*, 2010, **20**, 1722.
33 Y. Liu, X. Wang, Y. Dong, Z. Wang, Z. Zhao, J. Qiu, *J. Mater. Chem.* A, 2014, **2**, 16832.
34 X. Li, H. Wang, J. T. Robinson, H. Sanchez, G. Diankov, H. Dai, *J. Am. Chem. Soc.*, 2009, **131**, 15939.
35 I. Y. Jeon, H. J. Choi, M. J. Ju, I. T. Choi, K. Lim, J. Ko, H. K. Kim, J. C. Kim, J. J. Lee, D. Shin, S. M. Jung, J. M. Seo, M. J. Kim, N. Park, L. Dai, J. B. Baek, *Sci Rep.*, 2013, **3**, 2260.
36 T. A. Schaedler, A. J. Jacobsen, A. Torrents, A. E. Sorensen, J. Lian, J. R. Greer, L. Valdevit, W. B. Carter, *Science*, 2011, **334**, 962.
37 L. Wang, Y. Zhao, J. Wang, X. Hong, J. Zhai, L. Jiang, F. Wang, *Appl. Surf. Sci.*, 2009, **255**, 4944.
38 Z. Xue, S. Wang, L. Lin, L. Chen, M. Liu, L. Feng, L. Jiang, *Adv. Mater.*, 2011, **23**, 4270.
39 S. Wang, K. Liu, J. Liu, Z. T. F. Yu, X. Xu, L. Zhao, T. Lee, E. K. Lee, J. Reiss, Y. K. Lee, *Angew. Chem. Int. Ed.*, 2011, **50**, 3084.
40 Y. Tian, B. Su, L. Jiang, *Adv. Mater.*, 2014, **26**, 6872.
41 Q. Zhou, Z. Zhao, Z. Wang, Y. Dong, X. Wang, Y. Gogotsi, J. Qiu, *Nanoscale*, 2014, **6**, 2286.
42 W. H. Shin, H. M. Jeong, B. G. Kim, J. K. Kang, J. W. Choi, *Nano Lett.*, 2012, **12**, 2283.
43 K. Chang, D. Geng, X. Li, J. Yang, Y. Tang, M. Cai, R. Li, X. Sun, *Adv. Energy Mater.*, 2013, **3**, 839.
44 X. Li, J. Liu, Y. Zhang, Y. Li, H. Liu, X. Meng, J. Yang, D. Geng, D. Wang, R. Li, X. Sun, *J. Power Sources*, 2012, **197**, 238.
45 H. Wang, C. Zhang, Z. Liu, L. Wang, P. Han, H. Xu, K. Zhang, S. Dong, J. Yao, G. Cui, *J. Mater. Chem.*, 2011, **21**, 5430.
46 J. Lin, Z. Peng, C. Xiang, G. Ruan, Z. Yan, D. Natelson, J. M. Tour, *ACS Nano*, 2013, **7**, 6001.
47 C. Masarapu, V. Subramanian, H. Zhu, B.Wei, *Adv. Funct. Mater.,* 2009, **19**, 1008.
48 W. Lv, Z. Li, G. Zhou, J. J. Shao, D. Kong, X. Zheng, B. Li, F. Li, F. Kang, Q. H. Yang, *Adv. Funct. Mater.*, 2014, **24**, 3456.
49 S. Yang, Y. Cai, Y. Cheng, C. V. Varanasi, J. Liu, *J. Power Sources*, 2012, **218**, 140.
50 H. Hu, L. Yu, X. H. Gao, Z. Lin, X. W. Lou, *Energy Environ. Sci.* 2015, **8**, 1480.
51 W. B. Wan, L. L. Li, Z. B. Zhao, H. Hu, X. J. Hao, D. A. Winkler, L. C. Xi, T. C. Hughes, J. S. Qiu, *Adv. Funct. Mater.*, 2014, **24**, 4915.